Improving the Optical Yield of a Portable Plastic-Scintillator-Based Muon Tomography System

Kenneth Moats
Zernam Enterprises Inc

Prepared By:
Zernam Enterprises Inc
1701 Woodward Dr, Suite 110
Ottawa ON K2C 0R4

PWGSC Contract Number: W7714-45013443304

Technical Authority: David Waller, Defence Scientist, DRDC – Ottawa Research Centre.

Contract Report
DRDC-RDDC-2016-C142
April 2016

Improving the Optical Yield of a Portable Plastic-Scintillator-Based Muon Tomography System

Kenneth Moats

Contract Report

DRDC Ottawa

April 2016

Abstract

A portable muon tomography system could be used to image suspect Special Nuclear Material (SNM) objects that are approximately 1 m^3 or smaller. The work in this report focuses on the simulation and laboratory studies of this system for use by the Canadian Armed Forces (CAF). The main challenge for image reconstruction in a portable muon scattering tomography is achieving a precise angular resolution. In order to do so, the optical yield must be improved over that from the much larger CRIPT experiment.

This work studied seven materials that could be used as optical couplers, inserted between the plastic triangular scintillating bars and the wavelength shifting fibres. This would serve to minimize losses of scintillation photons as they are channeled by the wavelength shifting fibres via total internal reflection. Test data for this system using ^{90}Sr, ^{137}Cs and cosmic ray muon sources was collected at DRDC Ottawa Research Centre and was analyzed by writing C++ code using the ROOT analysis package. An optical simulation of the same system was performed using the C++ Geant4 framework as a means to validate the experimental results using cosmic ray muons. Although the Geant4 results for some optical couplers agree quite well with experiment, there are some discrepancies for the other optical couplers. Whether these discrepancies are due to limitations in the simulation or systematic errors in the experimental setup is currently being investigated.

Once the best optical coupler is determined, future simulations will allow us to

optimize design of the portable system and build a prototype for scanning 1 m^3 objects, which is currently in the preliminary design stages. Improving the muon position resolution will allow smaller muon trackers without sacrificing angular resolution. This work will allow us to determine if a plastic scintillator based portable muon tomography system is feasible and if it will meet user requirements for use in the field.

Table of Contents

List of Tables

List of Figures

Chapter 1

Introduction

The objective of the Special Nuclear Material (SNM) detection work being conducted at Defence Research and Development Canada (DRDC) is to develop technologies that improve the Canadian Armed Forces (CAFs) ability to detect SNM. Muon tomography work began at DRDC Ottawa Research Centre (ORC) in 2009 with project CRTI 08-0214RD [1]. A large muon tomography prototype was developed for these projects.

1.1 Muon Tomography and the CRIPT Experiment

The Cosmic Ray Inspection and Passive Tomography (CRIPT) project team built and tested a proof-of-concept, fixed-point detection system for border screening and non-proliferation applications. The CRIPT experiment employs naturally-occurring radiation (muons from cosmic rays) for detecting SNM and other high-density, high-atomic-number (high-Z) materials. Muon tomography relies on two or more planes of position sensitive muon detectors arranged above and below a volume to be imaged, potentially containing SNM or dense shielding material [2]. The upper detector layer measures the position and angle of the incoming muon tracks. As the muons pass

through the volume, they are deflected from multiple Coulomb scattering much more by SNM or dense shielding material than by low-density, low-Z materials. As the lower detector layer measures the position and angle of the outgoing muon tracks, measuring muon scattering through cargo containers allows reconstructing images of objects inside, and thus identifying potential threats involving SNM.

The multiple Coulomb scattering angles in muon tomography are sampled from a distribution that is assumed to be Gaussian. Although the actual distribution has heavier tails than a Gaussian, this is a good approximation for the central $\sim 98\%$ of scattering angles. This distribution has a mean scattering angle of zero degrees, and a width, in mrad, of

$$\theta_{MS} = \frac{13.6}{\beta pc}\sqrt{\frac{L}{X_0}}\left[1 + 0.038\ln\left(\frac{L}{X_0}\right)\right] \text{ mrad} \tag{1.1}$$

where β is the velocity of the muon as a fraction of the speed of light, c, p is the muon momentum in MeV/c, L is the path length of the muon through the material, and X_0 is the radiation length of the material [3]. The radiation length (in cm) is related to the density ρ (in g/cm^3), and atomic properties of the material by

$$X_0 = \frac{716.4\ A}{\rho Z(Z+1)\ln(287/\sqrt{Z})} \tag{1.2}$$

where Z is the number of protons per nucleus and A is the number of nucleons per nucleus [3]. It is evident that muons are deflected much more by high-Z SNM or dense shielding material than by low-density, low-Z materials. As an example, for muons with 1 GeV/c momentum traversing a 10 cm thickness of material, $\theta_{MS} = 14$ mrad for aluminum (Al), $\theta_{MS} = 35$ mrad for iron (Fe), $\theta_{MS} = 64$ mrad for lead (Pb), and $\theta_{MS} = 86$ mrad for uranium (U). Using sophisticated reconstruction techniques, the shape and composition of materials traversed by muons can be deduced by a

high-statistics measurement of the deflection angles [4].

The CRIPT detector system uses four planes of extruded plastic, triangular scintillator bars manufactured at Fermilab [5] for the MINERνA neutrino detector [6, 7]. Each panel has 121 triangular strips with a length of 2 m. The entire CRIPT detector is roughly 6 metres tall and weighs 22 tonnes. The CRIPT experiment achieved position resolution on the order of 3.5 mm with relatively short scanning times of ~ 60 seconds that are required for efficient scanning at border crossings. Obtaining high enough statistics to achieve good position resolution, and hence precise enough angular resolution to reconstruct a detailed image with these short scanning times is the most difficult challenge for muon tomography. The CRIPT experiment achieved angular resolutions of ~ 7 mrad, with a high true positive fraction of $\gtrsim 90\%$ with a low false positive fraction $\lesssim 10\%$ [1, 8, 9].

1.2 A Portable Muon Tomography Experiment

The potential for military applications of muon tomography was identified during the execution of the CRIPT project. A much smaller, portable system could be used to image suspect SNM objects that are approximately 1 m^3 or smaller. The current DRDC effort focuses on simulation and laboratory studies of a smaller, portable muon tomography system for use by the CAF. The system will use two trackers, each with a detector area of ~ 1 m^2 and a height of ~ 40 cm. In order for a pair of soldiers to carry the system into the field relatively easily, the weight of each tracker must be a maximum of ~ 100 kg.

One advantage of this smaller detector is that the imaging times can be much longer than at a border crossing, on the order of a few hours, which avoids the most difficult challenge that the CRIPT experiment faced. On the other hand, the challenge for portable muon scattering tomography is achieving an adequate angular

resolution. The new system's angular resolution for muon tracks should be similar to CRIPT's: $\sigma_{\theta_{x-z}} = 7$ mrad for a 2-dimensional scattering angle resolution in the $x-z$ plane (the y-direction is vertical). CRIPT's upper and lower tracking layers are 100 cm apart, so the position resolution for the portable system must be better to achieve the same angular resolution. The goal is to achieve a position resolution of $\sigma_x \simeq (40 \text{ cm}/100 \text{ cm}) \times 3.5 \text{ mm} = 1.4 \text{ mm}$.

The portable muon detection system will use the same triangular plastic scintillator bars as the CRIPT experiment, but with a length of 1 m or 0.75 m, instead of 2 m. These bars are composed of a base plastic of polystyrene (Dow Styron 663, chemical formula $(C_8H_8)_n$) doped with 2,5-diphenyloxazole (PPO, chemical formula $C_{15}H_{11}NO$) at a concentration of 1% by mass and a secondary dopant of 5-Phenyloxazole-2-yl (POPOP, chemical formula $C_{24}H_{16}N_2O_2$) at a concentration of 0.03% by mass. The bars are coated with a white co-extruded 0.25 mm TiO_2 reflective coating, composed of 15% TiO_2 (rutile) in polystyrene. The density of the strips is approximately 1.2 g/cm^3.

As a charged muon traverses the scintillator bar, it leaves behind it a wake of excited molecules in the base plastic, which release a small fraction of this energy as UV photons with short attenuation lengths (several mm). Longer attenuation lengths are obtained by dissolving the primary fluor (PPO), which is selected to efficiently re-radiate absorbed energy at wavelengths ($\sim$ 350 nm) where the base is more transparent. The primary fluor can also shorten the decay time by an order of magnitude (from $\sim$ 10 ns to $\sim$ 1 ns) and increase the total light yield through a resonant dipole-dipole interaction which efficiently transfers energy from the base to the fluor. As the absorption and emission spectra of the primary fluor have some overlap, to avoid self-absorption of photons in the primary fluor, the secondary fluor (POPOP) acts as a wavelength shifter, absorbing the UV photons and re-emitting

them as blue light ($\sim$ 400 nm). This increases the attenuation length of the scintillator bars.

To further increase the attenuation length and channel the scintillated light, wavelength shifting (WLS) fibres are inserted along the length of the bars through their centres. Kuraray Y-11 multi-clad wavelength shifting fibres [10] of diameter 1.2 mm are used to shift the scintillation photons to green light for detection with a Photomultiplier Tube (PMT) or Silicon Photomultiplier (SiPM) mounted at each end of the fibres in each bar.

For CRIPT's 64-channel Hamamatsu H8804 PMTs [11], an optical yield of roughly 10 photoelectrons per cm was obtained. These photon statistics dominate the position uncertainty, so for the smaller portable system, more light must be detected. Therefore, for the portable system, the PMTs were replaced by Hamamatsu S12572-050C SiPMs [11], because of a higher photon detection efficiency (35% vs. 15% for the PMTs at 500 nm). These SiPMs are attached to both ends of the fibres. To reduce blue and UV light losses from the scintillator-air-WLS fibre interfaces via total internal reflection, an optical coupler was inserted into the gap between the fibre and the scintillator bars. Since the scintillator bars have an index of refraction of $n_{sc} = 1.59$ and the WLS fibre has indices of refraction of $n_{WLS} = 1.59, 1.49, 1.42$ for the fibre core, inner cladding and outer cladding, respectively, the index of refraction of the optical coupler in the gap should be in the range $1.42 < n_{gap} < 1.59$, but ideally $n_{gap} \simeq 1.50$. To this end, a list of optical couplers to be studied is shown in Table 1.1.

The goal of this work is to determine the most effective optical coupler. That is, the material that produces the highest optical gain. Determining this material is crucial to improving the resolution of a portable muon tomography system. In Chapter 2, we present data that was collected at DRDC Ottawa Research Centre

Table 1.1: Optical couplers studied in this work.

Optical Coupler	Type	Manufacturer	Index of Refraction
BC630	Silicone Optical Grease	St. Gobain [12]	1.47
EJ550	Silicone Optical Grease	Eljen [13]	1.46
EJ552			1.47
NOA63	Optical Adhesive	Norland [14]	1.56
NOA68			1.54
NOA72			1.56
Water	Water	N/A	1.33

to test the optical couplers in Table 1.1, and we analyze this data to determine the measured optical gain for each material. In Chapter 3 we present the results of a Monte Carlo simulation of this system using the Geant4 simulation package. We use these results to determine the most promising materials to use as optical couplers in the portable muon tomography system. We summarize our conclusions in Chapter 4.

Chapter 2

Test Data

Four 45-cm long triangular plastic scintillator bars with Kuraray Y-11 1.2 mm diameter multi-clad WLS fibres along their centres were sealed in a light-tight box. To measure the light output at the ends of the fibres, Hamamatsu S12572-050C SiPMs were connected to a Vertilon SIB-108 board and a Vertilon IQSP482 charge integrating data acquisition (DAQ) system [15]. The experimental setup is shown in Figures 2.1 and 2.2.

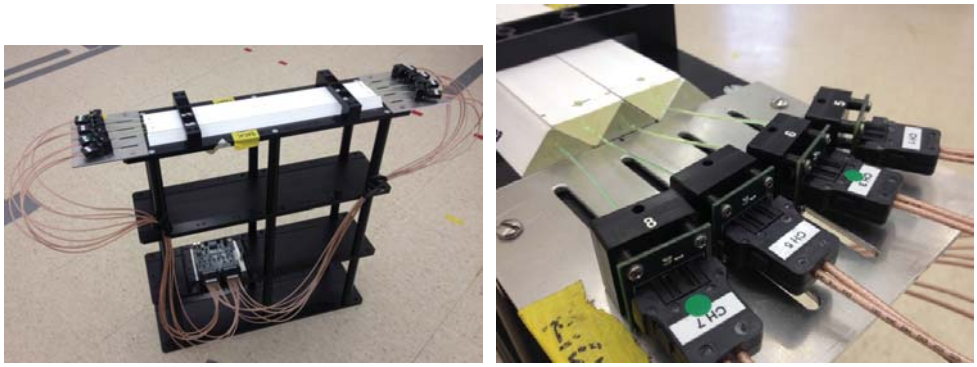

Figure 2.1: Four 45-cm long triangular plastic scintillator bars with Kuraray Y-11 1.2 mm diameter WLS fibres along their centres. Both ends of each fibre were connected to Hamamatsu S12572-050C SiPMs connected to a Vertilon SIB-108 board and a Vertilon IQSP482 charge integrating DAQ.

In addition to muons, two other sources were used: ^{90}Sr and ^{137}Cs. The ^{90}Sr and

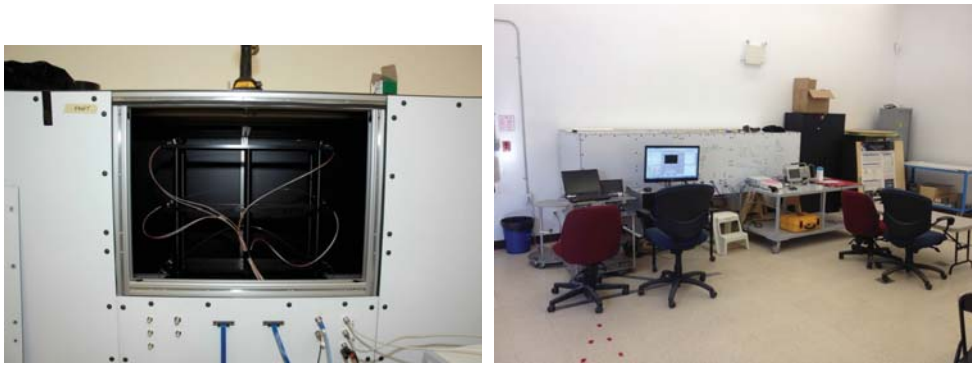

Figure 2.2: The scintillator bars were sealed in a light-tight box at DRDC Ottawa Research Centre.

^{137}Cs sources were fitted into a source holder having 3 mm thick lead shielding with a 2 mm diameter hole at the bottom. Magnets were used to suspend the source holder form the top of the dark box. The ^{90}Sr holder was positioned above bars 1 and 3, while the ^{137}Cs source was positioned above bar 2. Five positions along the bars were considered for the ^{90}Sr sources to test the light attenuation in the WLS fibre. All four bars were used for the muon runs.

Data was collected for 30 seconds for the ^{90}Sr runs, 60 seconds for the ^{137}Cs runs, and overnight ($\gtrsim$ 8 hours) for the muon runs. Once the data was obtained it was analyzed in several steps using C++ code written with ROOT version 5.34.34 [16]. First, a temperature correction was applied to the SiPM gain, as given by the manufacturer [11]:

$$\begin{aligned} \text{Gain} &= 1.25 \times 10^6 \\ \text{Temperature Coefficient of Gain} &= 2.7 \times 10^4/^\circ\text{C} \end{aligned} \tag{2.1}$$

Therefore, the temperature correction factor was applied to the measured charge as

$$\frac{\text{Temperature Coefficient of Gain}}{\text{Gain}} = 0.0216/^{\circ}C \tag{2.2}$$

The SiPMs at each end of the bars were labelled with a channel number as follows, as shown in Figure 2.1:

- Bar 1: Channels 1 and 2
- Bar 2: Channels 3 and 4
- Bar 3: Channels 5 and 6
- Bar 4: Channels 7 and 8

Once the data were obtained and the temperature correction was applied, there were two criteria that the events were required to satisfy. First, we applied a trigger requirement that the charge output at the end of a bar must be greater than 1.5 pC, otherwise the event was rejected. Second, we expect a correlation between the light output at one end of a given bar and the light output at the other end. Therefore, we rejected events that did not satisfy the coincidence requirement:

$$\begin{aligned}&\text{(Ch. 1 AND Ch. 2) OR (Ch. 3 AND Ch. 4)}\\ &\text{OR (Ch. 5 AND Ch. 6) OR (Ch. 7 AND Ch. 8)}\end{aligned} \tag{2.3}$$

The temperature corrected charge distributions for all ^{90}Sr, ^{137}Cs and muon runs were plotted for empty runs, in which no optical couplers were used, and also for the corresponding runs in which an optical coupler was inserted between the bar and the WLS fibre. For examples, see Figures 2.3-2.10. We wish to use these charge distributions to estimate the optical gain achieved by using each optical coupler.

The challenge in doing so is that one cannot simply count the number of events in these histograms and compute their ratio to determine the optical gain. This is mainly because adding an optical coupler pushes a larger fraction of the total number of collected events above the 1.5 pC threshold to pass the trigger condition. If one could reconfigure the positions of the bars so that the charge trigger is not applied to the bar whose optical coupler is being studied, then this would simplify the analysis. A solution to this is currently being investigated.

However, the shape of the high-charge tail should not be affected by the trigger condition. If one assumes that an exponential decay curve can be fit to these tails, the fit function is of the form:

$$N = N_0 e^{-q/\lambda} \tag{2.4}$$

where q is the charge of the events in the distribution and λ is the decay constant. Since these plots use a logarithmic scale on the y-axis, this can be rewritten as:

$$\log_{10}(N) = \log_{10}(N_0) - \log_{10}(e)q/\lambda \tag{2.5}$$

On a log scale, the tail of the charge distributions should therefore be linear with a negative slope proportional to $1/\lambda$. One can then compute the ratio of the decay constants, for runs with and without optical couplers, to estimate the optical gain. Alternatively, if one fits a linear function to the tail of the distribution, then the ratio of the fitted slopes is an estimate of the optical gain:

$$\text{Optical Gain} = \frac{m_{oc}}{m_{empty}} \tag{2.6}$$

where m_{oc} is the fitted slope for the distribution with an optical coupler, and m_{empty} is the fitted slope for the corresponding empty run without an optical coupler.

Care must be taken to use an appropriate range for the linear fit to accurately fit

the tail of the distribution. The lower and upper limits of this range were chosen to be the charge corresponding to 90% of the peak height and 30% of the peak height, respectively. The following algorithm was used to determine the range corresponding to the best linear fit to the charge distribution:

1. Perform a linear fit with the chosen range of histogram bins using the Fit() function in ROOT.

2. Compute the reduced chi-squared for the fit: $\tilde{\chi}^2 = \chi^2/N_{dof}$ where the chi-squared, χ^2, and the number of degrees of freedom, N_{dof}, were computed with the ROOT functions GetChisquare() and GetNDF(), respectively.

3. Move the lower endpoint to the right by one bin and move the upper endpoint to the left by one bin.

4. Repeat steps 1 to 3 until $\tilde{\chi}^2 < 2$. The fitted value of the slope has now been calculated for the resulting range of bins in the tail of the charge distribution.

This algorithm was performed for the runs with optical couplers and the corresponding empty runs, and Equation 2.6 was used to estimate the optical gain for all combinations of optical couplers, source types and source positions. The optical gain for each optical coupler and source type, averaged over channel number for ^{137}Cs and muons, and over source position and channel number for ^{90}Sr, is shown in Table 2.1. The quoted uncertainties are purely statistical, assuming Poisson statistics.

We see an encouraging ^{90}Sr response to the NOA68 optical coupler (see Figure 2.3), with an optical gain of 1.44 ± 0.04, and for water (see Figure 2.4), with an optical gain of 1.43 ± 0.02. We see a less encouraging optical gain for ^{90}Sr using other optical couplers, such as EJ552 (see Figure 2.5) and NOA72 (see Figure 2.6), with optical gains of 1.15 ± 0.02 and 1.16 ± 0.01, respectively. Similar results were obtained for

Table 2.1: Measured optical gain for each optical coupler and source type used in this study.

Optical Coupler	Optical Gain		
	^{90}Sr	^{137}Cs	Muons
BC630	1.20 ± 0.01	1.24 ± 0.01	1.38 ± 0.03
EJ550	1.26 ± 0.02	1.23 ± 0.01	1.34 ± 0.01
EJ552	1.15 ± 0.02	1.04 ± 0.02	1.32 ± 0.01
NOA63	1.37 ± 0.02	1.37 ± 0.02	1.45 ± 0.03
NOA68	1.44 ± 0.04	1.44 ± 0.03	1.73 ± 0.03
NOA72	1.16 ± 0.01	1.10 ± 0.01	1.22 ± 0.02
Water	1.43 ± 0.02	1.52 ± 0.02	1.73 ± 0.06

the ^{137}Cs data, with the best optical gains of 1.44 ± 0.04 for NOA68 (see Figure 2.7) and 1.43 ± 0.02 for water (see Figure 2.8).

For the purposes of this work, we are most interested in the optical gain using cosmic ray muons as a source. Slightly higher optical gains were obtained using muon data, with NOA68 (see Figure 2.9) and water (see Figure 2.10) producing the highest optical gains of 1.73 ± 0.03 and 1.73 ± 0.06, respectively. Once again EJ552 and NOA72 produced the worst optical gains of 1.32 ± 0.01 and 1.22 ± 0.02, respectively.

We have observed degradation and cracking of the bars with certain optical couplers, such as NOA68 and NOA72. For this reason, it is important to be more diligent in testing control bars periodically, to ensure the optimal performance of the bars. We also wish to validate these results using a Geant4 optical simulation. This is the focus of the next chapter.

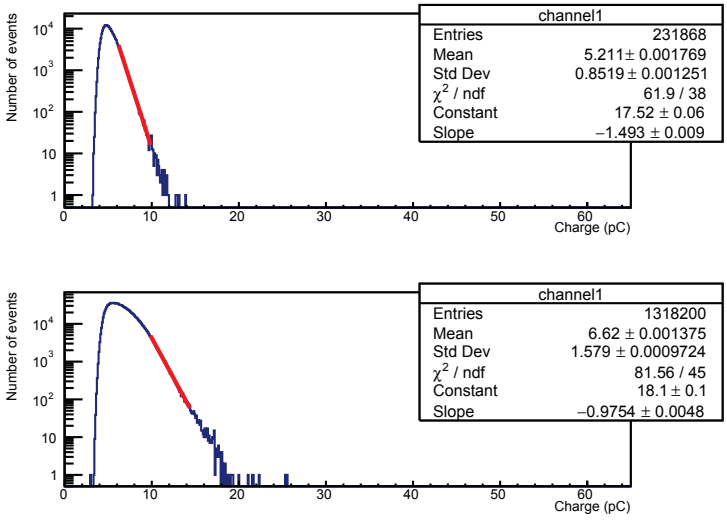

Figure 2.3: The NOA68 optical coupler was found to perform quite well using the ^{90}Sr source, with a measured optical gain of 1.44 ± 0.04. Empty run 149 is shown in the top figure and run 257 with NOA68 is shown in the bottom figure.

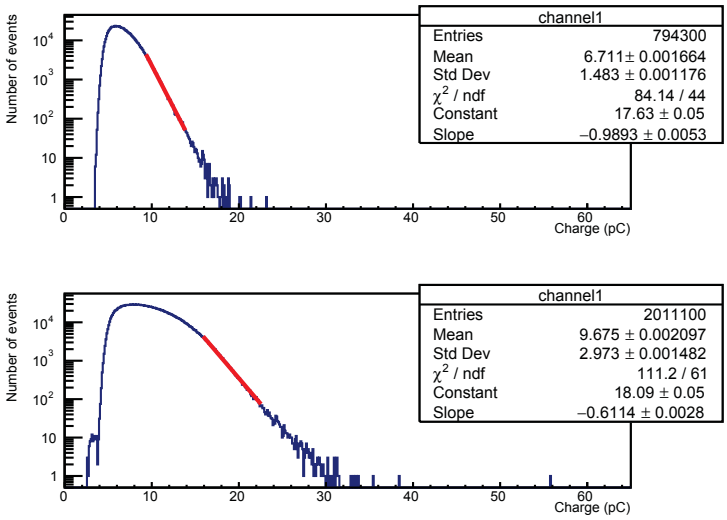

Figure 2.4: Water was found to perform quite well as an optical coupler using the ^{90}Sr source, with a measured optical gain of 1.43 ± 0.02. Empty run 223 is shown in the top figure and run 329 with water is shown in the bottom figure.

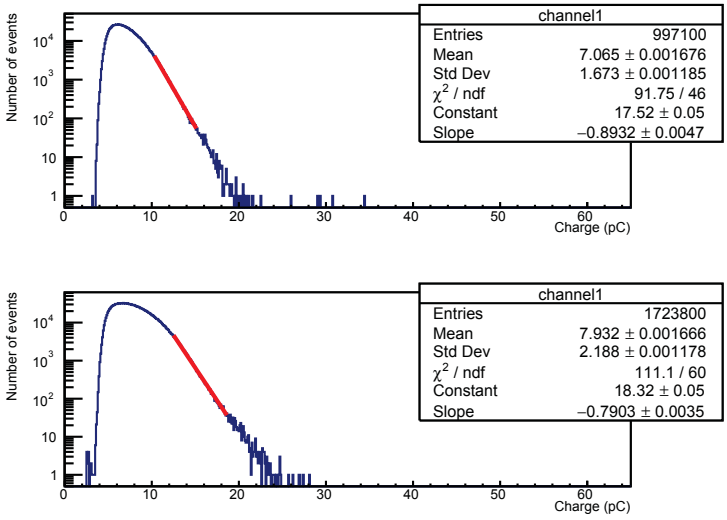

Figure 2.5: The EJ552 optical coupler was found to perform quite poorly using the ^{90}Sr source, with a measured optical gain of 1.15 ± 0.02. Empty run 365 is shown in the top figure and run 390 with EJ552 is shown in the bottom figure.

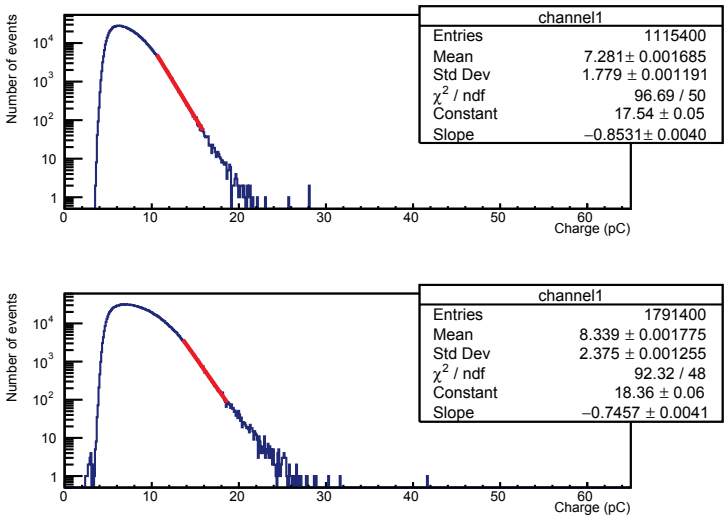

Figure 2.6: The NOA72 optical coupler was found to perform quite poorly using the ^{90}Sr source, with a measured optical gain of 1.16 ± 0.01. Empty run 414 is shown in the top figure and run 449 with NOA72 is shown in the bottom figure.

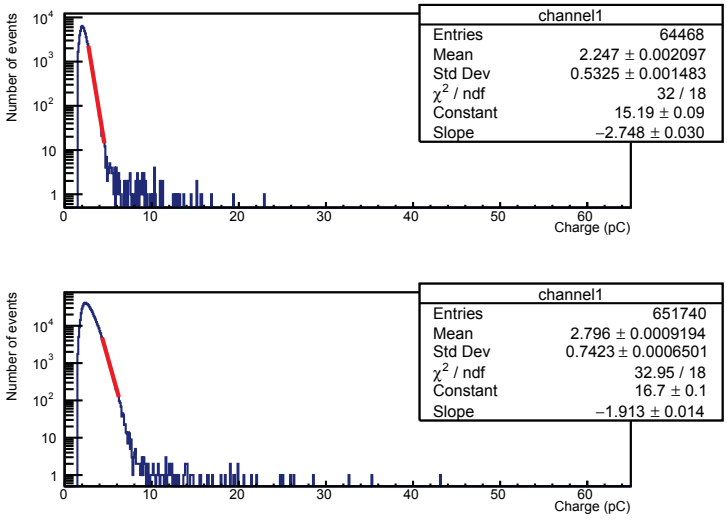

Figure 2.7: The NOA68 optical coupler was found to perform quite well using the ^{137}Cs source, with a measured optical gain of 1.44 ± 0.04. Empty run 157 is shown in the top figure and run 265 with NOA68 is shown in the bottom figure.

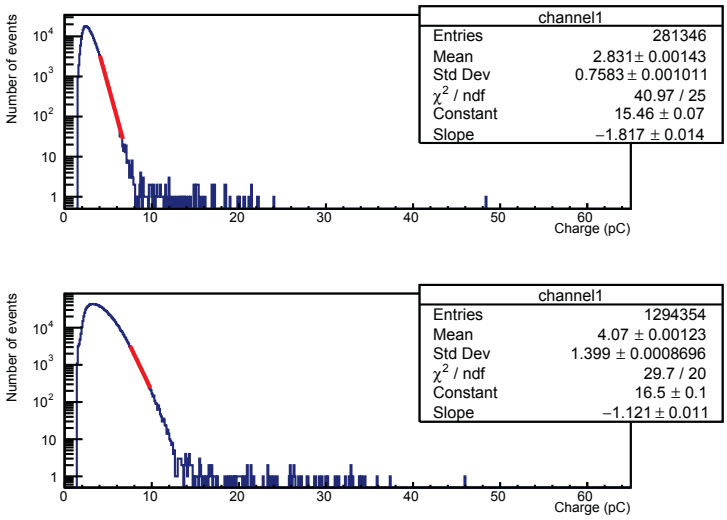

Figure 2.8: Water was found to perform quite well as an optical coupler using the ^{137}Cs source, with a measured optical gain of 1.43 ± 0.02. Empty run 220 is shown in the top figure and run 337 with water is shown in the bottom figure.

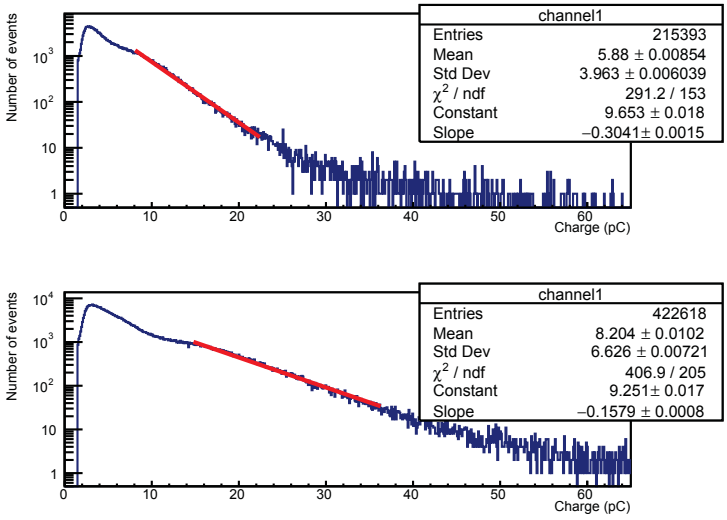

Figure 2.9: The NOA68 optical coupler was found to perform quite well using the cosmic ray muon source, with a measured optical gain of 1.73 ± 0.03. Empty run 158 is shown in the top figure and run 266 with NOA68 is shown in the bottom figure.

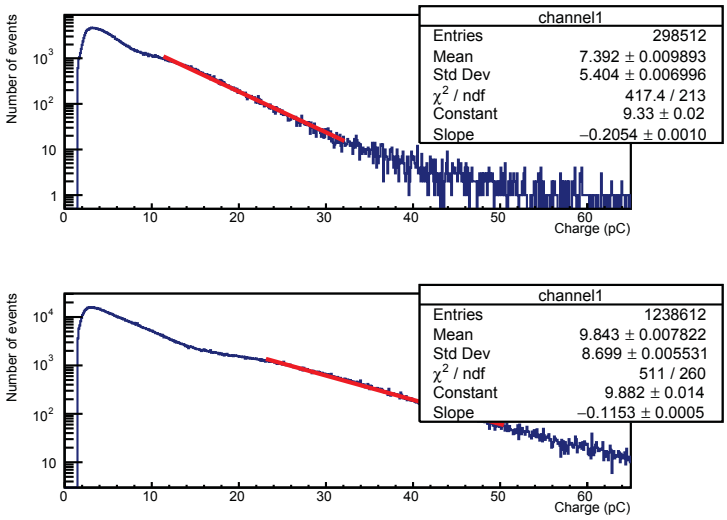

Figure 2.10: Water was found to perform quite well as an optical coupler using the cosmic ray muon source, with a measured optical gain of 1.73 ± 0.06. Empty run 219 is shown in the top figure and run 338 with water is shown in the bottom figure.

Chapter 3

Geant4 Simulation

3.1 CRY and Geant4

The Cosmic-RaY shower generator (CRY) is a fast cosmic-ray shower simulation tool which is based on precomputed input tables derived from full Monte Carlo N-Particle eXtended (MCNPX) simulations of 1 GeV to 100 TeV primary cosmic-ray particles on full atmosphere model [17]. It can generate correlated cosmic-ray particle showers at sea level, 2,100 m, and 11,300 m and be used as input to transport and detector simulation codes. Particles produced in the tool are muons, neutrons, protons, electrons, photons, and pions. In the study, we use CRY to generate only muons with energy larger than 1 GeV at sea level.

The simple setup using four triangular scintillating bars, as described in Chapter 2, can be simulated in detail within the Geant4 framework [18]. The performed simulation is based on a series of C++ classes, each responsible for a given step of the simulation, such as detector geometry and material building, particle and physics processes definition, particle tracking, hit definition and handling. In the following sections we describe in detail the main ingredients for these steps.

3.2 Physics and Optical Processes

Physics processes involved with interactions of high energy muons with matter include: ionization of high energy muons with radiative corrections, bremsstrahlung, electron-positron pair production, and muon induced nuclear reactions. Figure 3.1 shows the average energy loss of a muon in different materials from the contributions of these physics processes.

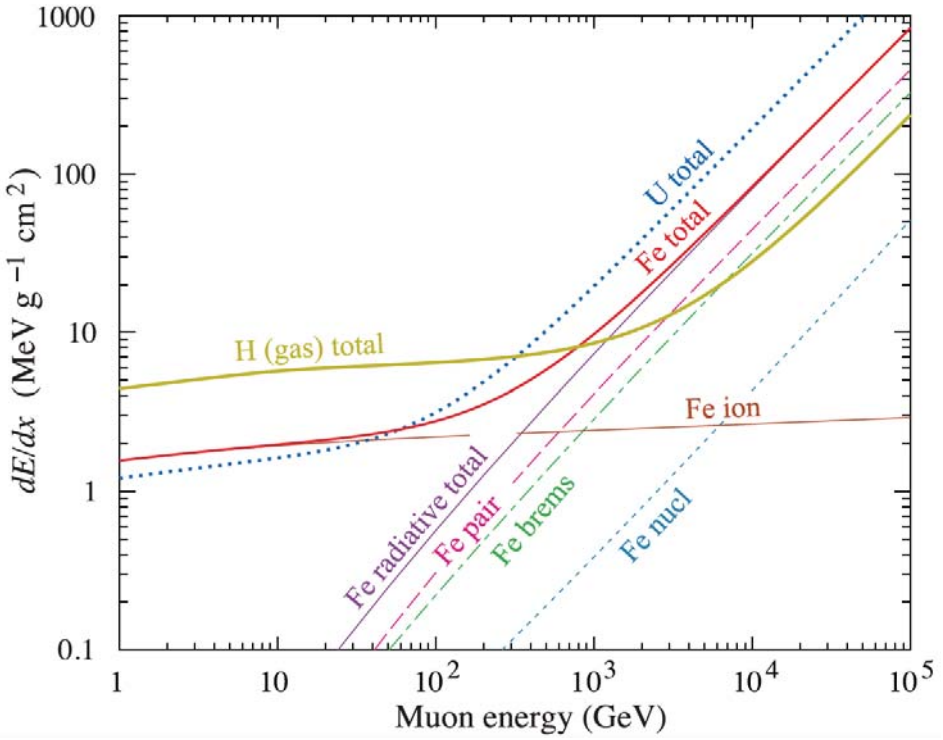

Figure 3.1: The average energy loss of a muon in hydrogen, iron, and uranium as a function of muon energy. Contributions to dE/dx in iron from ionization and radiative losses (e^+e^- pair production, bremsstrahlung and photonuclear interactions) are shown. For low energy muons, energy loss is dominated by ionization [3].

Below 200 GeV, muon energy losses are mainly due to ionization and the average loss is roughly 2 MeV/g cm^2. The processes have been implemented in the framework of the Geant4 toolkit [18] version 10.01.p02. Geant4 uses a set of Monte Carlo

simulation models which correspond to four Geant4 classes:

- G4MuIonization;
- G4MuBremsstrahlung;
- G4MuPairProduction;
- G4MuNuclearInteraction.

More detailed discussions on Geant4 muon physics processes can be found in Ref. [18]. In our study, we employ all the processes to simulate muon interactions with our detector materials and air.

All relevant physical and optical processes, as well as all particles involved, are defined in the PHYSICSLIST class. The former are standard electromagnetic processes, such as those shown in Figure 3.1. The optical processes include scintillation light generation, Cherenkov emission, bulk absorption, Rayleigh scattering, boundary processes (reflection, refraction, absorption) and the WLS process.

The existing CRIPT simulation code was made available and was modified to simulate the four triangular scintillating bars considered in Chapter 2. The muon physics processes had already been included in the PHYSICSLIST class. However, this code was modified to also include the optical processes necessary for a complete optical simulation of the WLS fibres, in particular:

- G4Scintillation
- G4OpWLS
- G4OpAbsorption
- G4OpRayleigh
- G4OpBoundaryProcess

As mentioned above, charged particles, traversing a thickness of a material, lose energy mainly by ionization. In Geant4, below a given energy threshold, the energy loss for $e^{\pm}$ or $\mu^{\pm}$ is treated as a continuous loss while above the threshold it is simulated by the explicit production of secondary particles. The scintillation mechanism is different in organic substances from inorganic ones. Certain types of materials, such as polystyrene, release a few percent of the absorbed energy as optical photons. The number of photons produced by charged particles is not linearly proportional to the energy loss, dE/dx, and can be described by Birk's semi-empirical formula

$$N = N_0 \frac{dE/dx}{1 + k_B dE/dx} \tag{3.1}$$

where N_0 is the photon yield at low specific ionization density, and k_B is Birk's density parameter, which for polystyrene-based scintillators is 0.126 mm/MeV. We assumed a scintillation yield of 10,000 optical photons per MeV and a scintillation time constant of 2.5 ns.

The particle tracks generated in the simulation can create hits in the scintillator strip and the SiPM that are defined in the BarHit and SiPMHit classes and handled by the SensitiveDetector class. A scintillator hit is created when the energy deposited in the bars by a track is not null. In this case, the energy deposition, vertex position, time, track ID and particle type are stored, together with the scintillator ID (bar number 1-4). A SiPM hit is created by optical photons reaching the photocathode of the SiPM. The number of photons for each generation process (scintillation, WLS emission) is stored, together with the photon position, arrival time, energy and SiPM ID (channel number 1-8).

3.3 Detector Construction and Optical Simulation

The detector design is modelled by the DETECTOR class, responsible for building the detector geometry, as well as all material bulk, and to set optical properties, such as scintillation characteristics, coating reflectivity, indices of refraction, etc. The geometry of the detector was modelled by four 45-cm-long triangular scintillator strips, extruded using Dow Styron 663 and doped with 1% PPO and 0.03% POPOP by mass. The dimensions of the triangular cross section of the bars is shown in Figure 3.2. The reflectivity of the TiO_2 reflective coating was assumed to be 100% for the purposes of this simulation.

The multi-clad WLS fibre (Kuraray Y-11 of diameter 1.2 mm) was inserted in the hole along the centre of each scintillator strip. The fibre was modelled by three concentric cylinders: core and cladding layers of different refraction indices (n_{core} = 1.59, $n_{clad,1}$ = 1.49, $n_{clad,2}$ = 1.42) with polished optical surfaces at each interface. Other interfaces (ground, back-painted, etc.) can be set as well. The various optical couplers, with refractive indices shown in Table 1.1, were inserted into the gap between the scintillator and WLS fibre and were also modelled using polished optical surfaces.

In order to simulate the readout of scintillation of light in a realistic scenario, the Hamamatsu S12572-050C SiPM, which was used for the experimental tests described in Chapter 2, was considered. To this aim, the SiPM was considered mounted to the fibre head-on at each end of the strip. The photocathode was treated as a sensitive volume and the cathode-fibre interface was treated as a dielectric-metal optical surface, set as polished. The reflectivity was considered to be zero, while the quantum efficiency (Q.E.) can be alternatively set to a fixed value or to a realistic wavelength-dependent spectrum. We chose the latter, using the spectrum shown in Figure 3.3

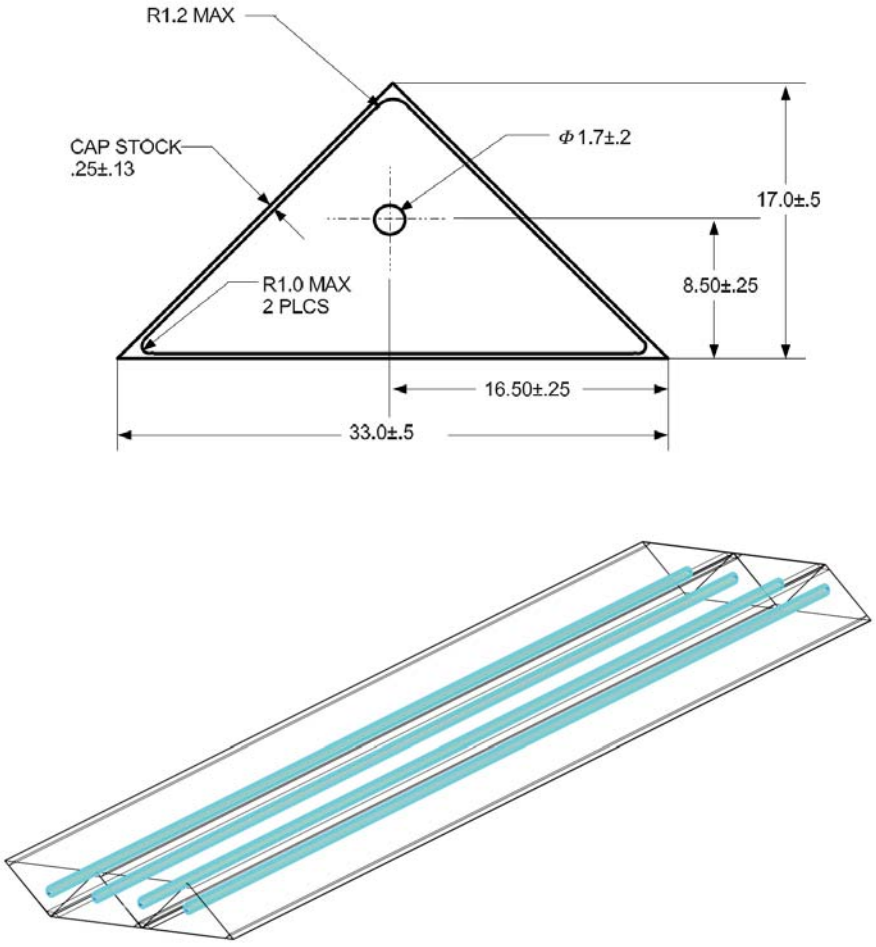

Figure 3.2: Dimensions of the triangular cross section of the scintillator bars, with a hole in the centre to hold the Kuraray Y-11 multi-clad WLS fibre. All dimensions are in mm. The figure on the bottom shows the configuration of the four 45-cm long bars and WLS fibres as constructed in Geant4.

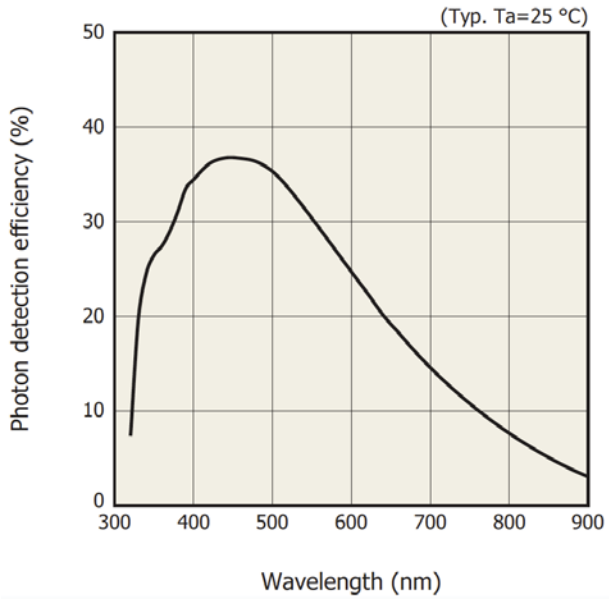

Figure 3.3: Wavelength-dependent quantum efficiency spectrum for the Hamamatsu S12572-050C SiPM [11].

3.4 Geant4 Optical Simulation Results

Several runs of the simulation were performed using the optical couplers shown in Table 1.1, inserted into the gap between the scintillator and WLS fibre. The number of muons incident on the bars was set to be 100,000. The number of optical photons for each SiPM channel and for each optical coupler are shown in Figure 3.4.

The total number of detected photons, for all eight channels summed together, are shown in Table 3.1 for each optical coupler run (N_{oc}) and for the corresponding empty run (N_{empty}). The corresponding optical gain is calculated as the ratio of detected photons with and without optical couplers (N_{oc}/N_{empty}) and is shown in the fourth column. The uncertainties given are purely statistical, assuming Poisson statistics. For comparison, the measured optical gain from the fourth column of Table 2.1 are shown.

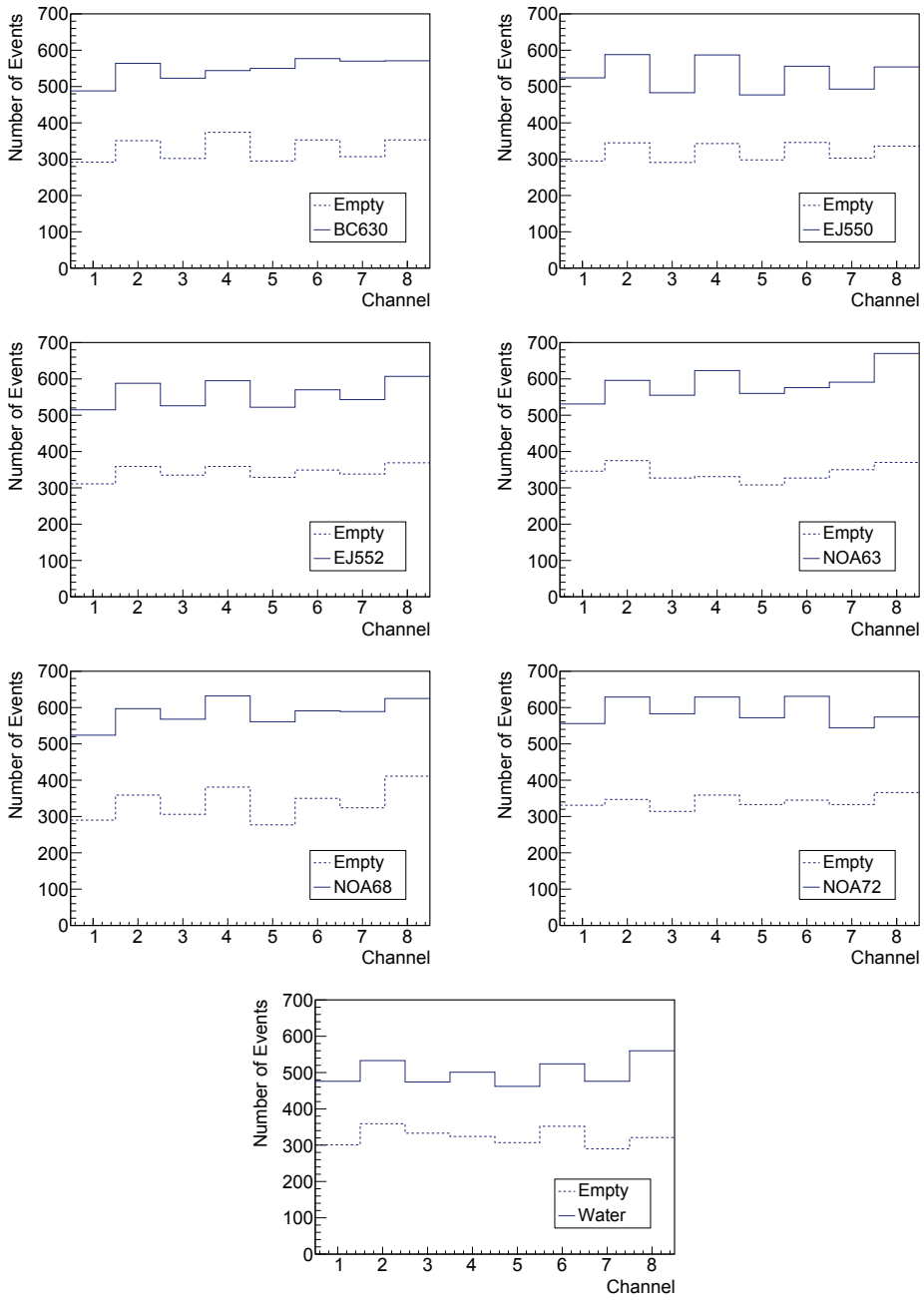

Figure 3.4: Number of optical photons detected by each SiPM (channel number) using all seven optical couplers from Table 1.1, shown as the solid lines. For comparison, the number of optical photons for the corresponding empty run, assuming an air gap between the scintillator and WLS fibre is shown as the dotted lines.

Table 3.1: Optical gain for each optical coupler from the Geant4 simulation using the CRY muon source. For comparison, the measured values of optical gain from the fourth column of Table 2.1 are shown.

			Optical Gain	
Optical Coupler	N_{oc}	N_{empty}	Geant4 Simulation	Data (Table 2.1)
BC630	4387 ± 66	2627 ± 51	1.67 ± 0.04	1.38 ± 0.03
EJ550	4262 ± 65	2557 ± 50	1.67 ± 0.04	1.34 ± 0.01
EJ552	4466 ± 67	2749 ± 52	1.62 ± 0.04	1.32 ± 0.01
NOA63	4702 ± 68	2734 ± 52	1.72 ± 0.04	1.45 ± 0.03
NOA68	4687 ± 68	2698 ± 52	1.74 ± 0.04	1.73 ± 0.03
NOA72	4718 ± 69	2728 ± 52	1.73 ± 0.04	1.22 ± 0.02
Water	4006 ± 63	2587 ± 51	1.55 ± 0.04	1.73 ± 0.06

3.5 Comparison of Test Data and Geant4 Simulations

It is evident from Table 3.1 that although the Geant4 simulation results agree quite well with the test data for the NOA68 optical coupler, there are some discrepancies for the other optical couplers. The Geant4 optical gains are generally larger than the measured values, with the exception being for water. It would be interesting to simulate the ^{90}Sr and ^{137}Cs sources in Geant4 to determine whether this discrepancy is present for those runs as well. It would also be interesting to use different optical surface models in Geant4 (i.e. ground instead of polished) to investigate whether the interface between the optical coupler and the scintillator bar and WLS fibre can be modelled more realistically. It is possible that the presence of air bubbles along these surfaces in the experimental setup may be able to account for this discrepancy.

Further study into these effects is needed to determine the best optical coupler, although based on these results, it seems that NOA68 is the most promising candidate for maximizing the optical gain of a portable muon tomography system.

Chapter 4

Summary

A portable muon tomography system could be used to image suspect SNM objects that are approximately 1 m^3 or smaller. The work in this report focused on the simulation and laboratory studies of this system for use by the CAF. The main challenge for image reconstruction in a portable muon scattering tomography is achieving a precise angular resolution. In order to do so, the optical yield must be improved over that from the much larger CRIPT experiment.

This work studied seven materials that could be used as optical couplers, inserted between the plastic triangular scintillating bars and the wavelength shifting fibres. This would serve to minimize losses of scintillation photons as they are channeled by the WLS fibres via total internal reflection. Test data for this system using ^{90}Sr, ^{137}Cs and cosmic ray muon sources was collected at DRDC Ottawa Research Centre and was analyzed by writing C++ code using the ROOT analysis package. It was found that the NOA68 optical coupler and water were the materials that maximized the optical gain compared to not using an optical coupler, as high as 1.73 ± 0.03 and 1.73 ± 0.06, respectively, for cosmic ray muons.

An optical simulation of the same system was performed using the C++ Geant4 framework as a means to validate the experimental results using cosmic ray muons. The Geant4 results for the NOA68 optical coupler agreed quite well with experiment,

with a simulated optical gain of 1.74 ± 0.04. However, there are some discrepancies for the other optical couplers. Whether these discrepancies are due to limitations in the simulation or systematic errors in the experimental setup is currently being investigated.

Another approach to confirm the measured and simulated light yields is to modify the configuration of bars and trigger. By placing the four bars in a pyramid configuration, this removes the test bar from the trigger requirement and allows one to use the external triggers with muon data. This will help confirm the best optical coupler that produces the highest optical gain. We also wish to use larger diameter optical fibers, namely the 1.5 mm and 2.0 mm St. Gobain fibres, which allow more optical photons to be collected and channeled to the SiPM.

Once the best optical coupler is determined and the larger fibres tested, we plan to measure the efficiency and resolution of 1 metre long bars with four layers (2 per tracker) of scintillators, using the best optical coupler and WLS fiber. This, along with future simulations will allow us to optimize design of the portable system and build a prototype for scanning 1 m^3 objects, which is currently in the preliminary design stages. Improving the muon position resolution will allow smaller muon trackers without sacrificing angular resolution. This work will allow us to determine if a plastic scintillator based portable muon tomography system is feasible and if it will meet user requirements for use in the field.

References

[1] D. Waller, *et al.* Close-out report for the Cosmic Ray Inspection and Passive Tomography (CRIPT) project [CRTI Project 08-0214RD]. *DRDC-RDDC-2014-R177*, 2014.

[2] K.N. Borozdin, G.E. Hogan, C. Morris, *et al.* Radiographic imaging with cosmic-ray muons. *Nature*, 422:277, 2003.

[3] K. A. Olive, *et al.* Review of Particle Physics. *Chin. Phys. C*, 38:090001, 2014.

[4] L.J. Schultz, *et al.* Image reconstruction and material Z discrimination via cosmic ray muon radiography. *Nucl. Inst. & Meth. in Phys. Res. A*, 519:687, 2004.

[5] M. Adams, N. Amos, D.A. Averill, *et al.* A new detector technique using triangular scintillating strips to measure the position of minimum ionizng particles. *Nucl. Inst. & Meth. in Phys. Res. A*, 378:131, 1996.

[6] A. Pla-Dalmau, A.D. Bross, V.V. Rykalin and B.M. Wood. Extruded plastic scintillator for minerva. *Technical report, Fermilab*, 2005.

[7] A. Pla-Dalmau, A.D. Bross and K.L. Mellott. Low-cost extruded plastic scintillator. *Nucl. Inst. & Meth. in Phys. Res. A*, 466:482, 2001.

[8] D. Bryman, Z. Liu and J. Bueno. Monte Carlo simulation of a prototype cosmic muon detector. *DRDC-RDDC CR 2010-209*, 2010.

[9] D. Waller. A simulation study of material discrimination using muon scattering tomography. *DRDC TM 2010-211*, 2010.

[10] Kuraray Plastic Scintillating Fibers, http://www.kuraray.co.jp/en/.

[11] Hamamatsu, http://www.hamamatsu.com/jp/en/.

[12] Saint-Gobain Crystals, http://www.crystals.saint-gobain.com/.

[13] Eljen Technology, http://www.eljentechnology.com/.

[14] Norland Products, http://www.norlandprod.com/.

[15] Vertilon, http://www.vertilon.com/.

[16] R. Brun and F. Rademakers. ROOT - An Object Oriented Data Analysis Framework. *Nucl. Inst. & Meth. in Phys. Res. A*, 389:81–86, 1997.

[17] C. Hagmann, *et al.* Cosmic-Ray Shower Library (CRY). *User Guide*, 2008.

[18] S. Agostinelli, *et al.* Geant4 - A Simulation Toolkit. *Nucl. Inst. & Meth. in Phys. Res. A*, 506:250–303, 2003.